Divergent growth of poly(amidoamine) dendrimer-like branched polymers at the reducing end of cellulose nanocrystals

Maud Chemin, Céline Moreau, Bernard Cathala, Ana Villares

To cite this version:

Maud Chemin, Céline Moreau, Bernard Cathala, Ana Villares. Divergent growth of poly(amidoamine) dendrimer-like branched polymers at the reducing end of cellulose nanocrystals. Carbohydrate Polymers, 2022, 279, pp.119008. 10.1016/j.carbpol.2021.119008 . hal-04193854

HAL Id: hal-04193854
https://hal.inrae.fr/hal-04193854v1

Submitted on 1 Sep 2023

Divergent growth of poly(amidoamine) dendrimer-like branched polymers at the reducing end of cellulose nanocrystals

Maud Chemin, Céline Moreau, Bernard Cathala, Ana Villares*

UR1268 BIA, INRAE, F-44316, Nantes, France

ABSTRACT

This paper presents the growth of dendritic polymers at the reducing ends of cellulose nanocrystals by the “grafting from” approach. We took advantage of the chemically differentiated ends of cellulose nanocrystals to specifically synthesize dendrimers at their reducing end by the divergent approach. We used acid-amine coupling reactions in aqueous media to synthesize the carboxylic acid- or amine-terminated poly(amidoamine) dendrimers. The growth of dendrimer generations was monitored by UV and FTIR spectroscopies, and we successfully introduced up to 4 generations. The dendrimer growth at reducing ends was demonstrated by the nanocrystal adsorption driven by the peripheral amino groups onto gold surfaces. Hence, the results from quartz crystal microbalance with dissipation (QCM-D) pointed to a rather upright orientation of the dendrimer-modified cellulose nanocrystals. As the generation increased, the adsorbed layers appeared to be more flexible, which demonstrated that the functionality at the reducing end can successfully tune the properties of cellulose nanocrystals.

Keywords: tunicate cellulose nanocrystals; reducing end functionalization; poly(amidoamine) dendrimer; oriented adsorption.

1. Introduction

Cellulose nanocrystals (CNC) have gained prominence as bio-based materials for a wide range of applications (Charreau, H., Cavallo, E., & Foresti, M. L., 2020) thanks to their mechanical and barrier properties, liquid crystal behavior, optical properties, and amphiphilic characteristics (Eichhorn, S. J., 2011; Heise, K. et al., 2020; Lin, N., Huang, J., Chang, P. R., Anderson, D. P., & Yu, J., 2011). CNC are obtained from cellulose fibers by acid hydrolysis that preferentially solubilizes the disordered regions of cellulose, resulting in rod-like crystallites with cross-sections in the nanoscale (5-20 nm) and aspect ratio values in the 5-50 range (Sacui, I. A. et al., 2014). One of the particularities of cellulose is the orientation of the chains within the crystal structure yielding two chemically differentiated ends. Indeed, the parallel arrangement of cellulose chains in the cellulose I allomorph results in C1 reducing ends (aldehyde functionalities) at one end of the nanocrystal, and C4 hydroxyl groups at the opposite end. Taking advantage of this chemical polarity (hydroxyl versus aldehyde), the selective modification of CNC reducing ends has recently attracted much attention (Heise, Katja et al., 2020; Tao, H., Lavoine, N., Jiang, F., Tang, J., & Lin, N., 2020) However, there are still very few studies focusing on the growth of functionalities at reducing ends by the "grafting from" approach (Delepierre, G. et al., 2021; Risteen, B. et al., 2018; Zoppe, J. O. et al., 2017). Generally, the polymerization initiator is introduced at the reducing end and the subsequent addition of the monomers yields to the polymeric functionality. This article describes for the first time the synthesis of poly(amidoamine) dendrimers at the CNC reducing ends by the "grafting from" approach. Our strategy involves straightforward acid-amine coupling reactions, and CNC act as solid support to immobilize the core and grow dendrimer generations.

Dendrimers are regular hyperbranched polymers synthesized from a multi-functional core by repeated cycles of synthesis. They are characterized by the number of branches (generation) and the peripheral functional groups (amino, carboxyl, hydroxyl or hydrocarbon groups). Therefore, dendrimers display multiple peripheral functional groups giving rise to multivalencies and a tunable size depending on dendritic generation. Hence, dendrimers have found many applications in different fields as nanoscaffolds for targeted drug delivery, and templates for the fabrication of metal nanoparticles (Guo, Y. Q., Shen, M. W., & Shi, X. Y.; Nikzamir, M., Hanifehpour, Y., Akbarzadeh, A., & Panahi, Y.). The grafting of dendrimers on cellulose offers many advantages resulting from its promising properties such as biodegradability, biocompatibility, and availability. Poly(propylene imine) (PPI) and poly(amidoamine) (PAMAM) dendrimers have been grown on the CNC surface by iterative Michael additions (Golshan, M., Salami-Kalajahi, M., Roghani-Mamaqani, H., & Mohammadi, M., 2017; Hassan, M. L., 2006; Tehrani, A. D. & Basiryan, A., 2015; Wang, Y. C. & Lu, Q. Y., 2020). In those studies, dendrimers covered the whole CNC surface and changed significantly their surface properties, inducing CNC aggregation. In this work, we specifically synthesized dendrimers at the CNC reducing end, thus retaining the CNC surface properties while adding the dendritic functionalities at one end. As previously showed, the introduction of functionalities at the CNC reducing ends allows the supramolecular assembly by this end, and tunes the responsiveness (Chemin, M., Moreau, C., Cathala, B., & Villares, A., 2020; Chemin, Maud, Moreau, Céline, Cathala, Bernard, & Villares, Ana, 2020; Lokanathan, A. R. et al., 2013; Villares, A., Moreau, C., & Cathala, B., 2018). This work opens new perspectives for CNC applications, by their patchy modification to achieve the desired functionality at the reducing end.

2. Materials and methods

2.1. Cellulose nanocrystals preparation

Cellulose nanocrystals (t-CNC) were obtained from tunicates (*Styela clava*) collected on the coast of Quimiac (France) and prepared and characterized as previously described (Chemin, M. et al., 2020; Chemin, Maud et al., 2020; Villares, A. et al., 2018). The surface charge density, calculated by conductometric titration (TIM900 titration manager and CDM230 conductimeter), was 0.022±0.001 mmol g^{-1}.

2.2. Materials

N-(3-dimethylaminopropyl)-*N*-ethylcarbodiimide hydrochloride (EDC), *N*-hydroxysuccinimide (NHS), hexamethylenediamine (HMDA) (98%), trimesic acid (TMA) (95%), sodium chlorite ($NaClO_2$), acetic acid, potassium chloride (KCl) and potassium hydroxide (KOH) were purchased from Sigma-Aldrich (France) and were used without further purification. Dialysis membrane, molar mass cut off 12-14 kDa, was purchased from Spectrum Laboratories Inc. Water was purified by Millipore Milli-Q purification system (18.2 MΩ).

2.3. Methods

2.3.1. Introduction of amine moieties.

Prior to the first step of functionalization, the aldehyde groups on the reducing end of t-CNCs were oxidized to carboxylic acid groups as previously described (Chemin, M. et al., 2020; Chemin, Maud et al., 2020; Villares, A. et al., 2018). Briefly, t-CNC (200 mL at 6.9 g L^{-1}) were oxidized by the addition of 33.7 mmol of $NaClO_2$, and the pH was adjusted to 3.5 using 1 M acetic acid, followed by stirring for 20 h at room temperature. The reaction mixture was purified by centrifugation (20000 g, 20 °C, 60 min) followed by dialysis (molar mass cut off 12-14 kDa) against milli-Q water for 10 days. Dispersions were stirred in water for 24 h to avoid nanocrystal aggregation.

Afterwards, amine moieties were introduced using the NHS/EDC amide coupling with hexamethylenediamine (Lokanathan, A. R., Lundahl, M., Rojas, O. J., & Laine, J., 2014). A 2 g L^{-1} suspension of oxidized t-CNC was degassed by bubbling nitrogen for 20 min, and NHS (50 mmol) was added, followed by EDC (5 mmol), and the pH was checked to be close to 6.5. Appropriate amounts of KCl were added such that the final suspension was 0.5 M. Hexamethylenediamine was added in large excess (5 mmol) to avoid the grafting of two t-CNCs on the same molecule. Then, pH was checked to be above 9.2. The reaction was incubated under magnetic stirring at room temperature for 24 h. Amine-functionalized t-CNCs were purified by centrifugation (20000 g, 60 min, 20 °C) and then dialyzed (molar mass cut off 12-14 kDa) against Milli-Q water for 5 days. After dialysis, dispersions were stirred in water for 24 h to avoid nanocrystal aggregation.

2.3.2. Introduction of acid moieties

A similar procedure was applied to graft trimesic acid on the amine-functionalized t-CNCs. Appropriate amounts of KCl were added to the suspension of amine-functionalized t-CNCs such that the final suspension was 0.5 M and the dispersion was stirred under nitrogen bubbling for 20 min. A 0.95 g L^{-1} solution of trimesic acid in water was degassed by bubbling nitrogen for 5 min, NHS were added (3 mmol), followed by EDC (15 mmol) under stirring and bubbling nitrogen. Both suspensions were then mixed with a final t-CNC concentration of 1.5 g L^{-1} (5 mmol of amine groups). pH was checked to be above 9.2, and the reaction was incubated under magnetic stirring at room temperature for 24 h. Acid-functionalized t-CNCs were purified by centrifugation (20000 g, 60 min, 20 °C) and then dialyzed (molar mass cut off 12-14 kDa) against Milli-Q water for 5 days. Dispersions were stirred in water for 24 h to avoid nanocrystal aggregation. After grafting, hybrid nanoparticles are denoted t-CNC-G*x*, *x* being the generation. When *x* is a decimal number, the peripheral groups are the carboxylic acid, and when *x* is an integer, the t-CNC peripheral groups are the amine functionalities. The step-by-step synthesis was repeated consecutively up to the synthesis of the fourth generation t-CNC-G4.

2.4. Characterization

2.4.1. Scanning Transmission Electron Microscopy (STEM)

t-CNC dispersions were diluted to 0.2 g L^{-1} in KOH 1 mM and deposited on freshly glow-discharged carbon-coated electron microscope grids (200 mesh, Delta Microscopies, France). Water excess was removed by blotting (Whatman filter paper). The grids were dried overnight in air at ambient temperature and then coated with platinum layer by an ion-sputter coater (thickness = 0.5 nm). The grids were observed with a Quattro Scanning electron microscopy (Thermo Scientific) with a STEM detector, working at 10kV.

2.4.2. Elemental analysis. t-CNCs were freeze-dried and the resulting powder (10 mg) was placed in tin capsules for analysis. The total C, N, and S contents of t-CNCs were determined by a C/N/S analyzer (Vario Micro cube, Elementar) coupled to a gas chromatographic system and a thermal conductivity detector (TCD). Nitrogen content was determined by the Dumas’ method combustion (Shea, F. & Watts, C. E., 1939).

2.4.3. Infrared spectroscopy

Infrared spectra were obtained from KBr pellets containing freeze-dried t-CNC and t-CNC-G*x* samples placed directly in a Nicolet iS50 FTIR spectrometer (Thermo Scientific) in absorbance mode. All spectra were recorded using OMNIC software with a 4 cm^{-1} resolution after 200 continuous scans from 400 to 4000 cm^{-1}. All samples were acidified with HCl 100 mM in order to protonate carboxylic acids.

2.4.4. UV-visible spectroscopy

UV-visible spectra were obtained from t-CNC-G*x* suspensions at 0.3 g L^{-1} in KOH 1mM using a quartz cell placed directly in a SPECORD S 600 spectrometer (Analytik Jena GmbH). All spectra were recorded using WinASPECT software set to absorbance mode after 10 accumulations and scanning from 200 to 1000 nm. A reference sample consisting of t-CNC at 0.3 g L^{-1} in KOH 1mM mixed with trimesic acid at 0.001 g L^{-1} in KOH 1 mM was used for comparison.

2.4.5. Thermal degradation

Thermogravimetric analysis (TGA) were performed under a nitrogen atmosphere using a TA instruments TGA2050. Samples (5 mg) were equilibrated at 60°C for 10 minutes and heated from 60 to 600 ºC at a heating rate of 5 ºC min^{-1}.

2.4.6. Surface Plasmon Resonance (SPR)

The SPR measurements were performed with a Biacore x100 (GE Healthcare, Sweden) with a continuous flow system. The SPR technique is based on the phenomenon of total internal reflection of light. The adsorption of dendrimer-modified t-CNC onto the sensor surface produces a shift in the optical resonance properties of the sensor, which results in an increase of the SPR angle where the reflected light intensity is in its minimum (Schoch, R. L. & Lim, R. Y. H., 2013). All measurements were carried out using gold sensors at 20 °C with a 0.3 g L^{-1} dispersion of t-CNC in KOH 1mM at 10 µL min^{-1}. The amount of adsorbed dendrimer-modified t-CNC, Γ, was then calculated from the SPR angle shift, $\Delta\theta$, according to the following expression (Kontturi, K. S., Kontturi, E., & Laine, J., 2013):

$$\Gamma = \frac{l_d}{2}\frac{\Delta\theta}{m(^{dn}/_{dc})} \tag{1}$$

Where l_d is the characteristic evanescent electromagnetic field decay length (281.2 nm), m is the sensitivity factor for the sensor (102.5º per RIU) obtained after calibration, and dn/dc is the refractive index increment (0.15 mL g^{-1}). Results are expressed as the mean of two experiments.

2.4.7. Quartz crystal microbalance with dissipation monitoring (QCM-D)

QCM-D measurements were performed with a Q-Sense E4 instrument (AB, Sweden) using a piezoelectric AT-cut quartz crystal coated with gold electrodes on each side (QSX301, Q-Sense), as previously described (Chemin, Maud et al., 2020; Villares, A. et al., 2018). All measurements were carried out using the QCM flow cell modules at 20 °C with a 0.3 g L^{-1} dispersions of t-CNC in KOH 1 mM at 100 µL min^{-1}. Frequency ($\Delta f_n/n$) and (ΔD_n) dissipation changes were simultaneously registered at 5 MHz fundamental resonance frequency and its several overtones as a function of time. Any material adsorbed on the crystal surface induces a decrease of the resonance frequency. If the adsorbed mass is evenly distributed, rigidly attached and small compared to the mass of the crystal, Δf is directly proportional to the adsorbed mass ($\Delta\Gamma$) using the Sauerbrey’s equation (Sauerbrey, G., 1959):

$$\Delta\Gamma = -C\frac{\Delta f}{n} \tag{2}$$

where C is the constant for the mass sensitivity of the quartz crystal (0.177 mg m^{-2} Hz^{-1} at $f_0 = 5$ MHz) and n is the overtone number.

Dissipation signals were recorded simultaneously to frequency shifts and they provide a measure of the frictional losses due to the viscoelastic properties of the adsorbed layer. The overtone $n = 5$ was used for comparing the adsorption of unmodified and modified t-CNCs.

3. Results

3.1. Dendritic synthesis at t-CNC reducing end

Cellulose nanocrystals can be viewed as rigid rod-like crystals with two chemically differentiated ends. Hence, reducing ends display aldehyde groups whereas the non-reducing ends present the less reactive hydroxyl groups. This chemical asymmetry allows the selective introduction of functionalities at the reducing end of cellulose nanocrystals (Lin, F., Cousin, F., Putaux, J.-L., & Jean, B., 2019; Lokanathan, A. R. et al., 2013; Villares, A. et al., 2018). In this work, we have used tunicate cellulose nanocrystals (t-CNC) as a solid support for the divergent synthesis of poly(amidoamine) dendrimers at the t-CNC reducing ends. Tunicate cellulose nanocrystals were selected because they are quasi-perfect monocrystals and, besides their narrow distribution in cross-section and length dimensions, they have a rectangular 8.8 nm × 18.2 nm cross-sectional shape (Terech, P., Chazeau, L., & Cavaille, J. Y., 1999). As the monomers, we selected a diamine, the hexamethylenediamine (HMDA), and a tricarboxylic acid, the trimesic acid (TMA). Therefore, dendrimer growth was driven by TMA, whereas the HMDA grafting only changed the peripheral functional groups.

Our synthetic approach first involved the oxidation of t-CNC aldehyde groups into carboxylic acids and the subsequent dendrimer growth by the *N*-(3-dimethylaminopropyl)-*N*-ethylcarbodiimide hydrochloride (EDC) chemistry. Fig. **1** shows the theoretical dendrimer generation growth at the reducing end of cellulose nanocrystals. EDC-activated carboxylic acids were transformed into amine functionalities by their reaction with hexamethylenediamine. HMDA was added in high excess to avoid cross-linking. Furthermore, reactions were carried out above pH 9.2 and at high ionic strength (KCl 0.5 M) to screen t-CNC interactions and avoid unspecific adsorption of chemicals. The second step was the reaction of amine-functionalized t-CNC with trimesic acid. Reaction was carried out under similar conditions, TMA was EDC-activated and added to amino-t-CNC dispersed in high ionic strength solutions (KCl 0.5 M) at pH 9.2. This two-step procedure was repeated 4 times to achieve the amine-terminated generation 4 (t-CNC- G4).

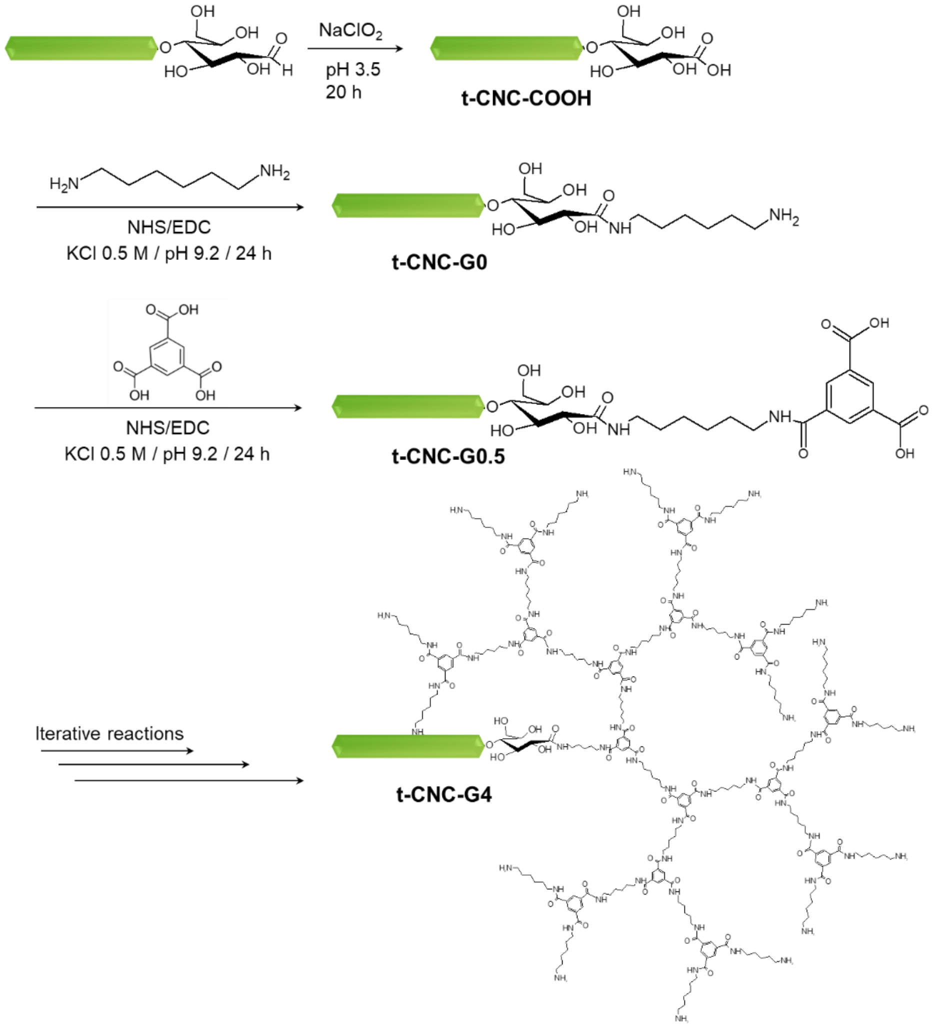

Fig. 1. Scheme of the divergent dendrimer synthesis on the reducing ends of t-CNC by the successive grafting of HMDA and TMA by EDC/NHS activation. In the scheme, t-CNC are represented as green rods. Dimensions of t-CNC, HMDA and TMA are not scaled.

Generally, poly(amidoamine) dendrimers are prepared by serial repetitions of the Michael addition of amine-functionalized CNCs (Golshan, M. et al., 2017; Hassan, M. L., 2006; Tehrani, A. D. & Basiryan, A., 2015). Recently, Wang et al. have described a protocol including a Michael addition followed by amination in methanol (Wang, Y. C. & Lu, Q. Y., 2020). However, in all cases, reactions were performed in methanol/water mixtures. Our approach involved successive amidation reactions with EDC/NHS activation and did not require the use of organic solvents or high temperatures. Reactions were entirely performed in aqueous media at room temperature. Purification and removal of soluble chemicals after each generation growth was facilitated by t-CNC precipitation. The high ionic strength (0.5 M) favored nanocrystal precipitation and then, salt was removed by dialysis. The recovered t-CNC masses after each reaction were higher than 99% for both the first oxidation and the successive EDC/NHS coupling. t-CNC-G*x* were stirred overnight in KOH 1 mM to avoid nanocrystal aggregation arising from the interaction between positively charged amino groups and the negative sulfate groups in the surface of t-CNC. As Fig. 2 shows, the morphology of t-CNC was not altered by the dendritic growth at their reducing ends, the t-CNC exhibited the typical and expected rod-like shape. The STEM images did not show significant differences between when the dendrimer was amino- or acid-terminated, and no significant association between nanocrystals was observed due to dendrimer growth. Hence, t-CNC can be viewed as a solid support to hold the dendrimer so the excess of chemicals can be easily removed by centrifugation and dialysis.

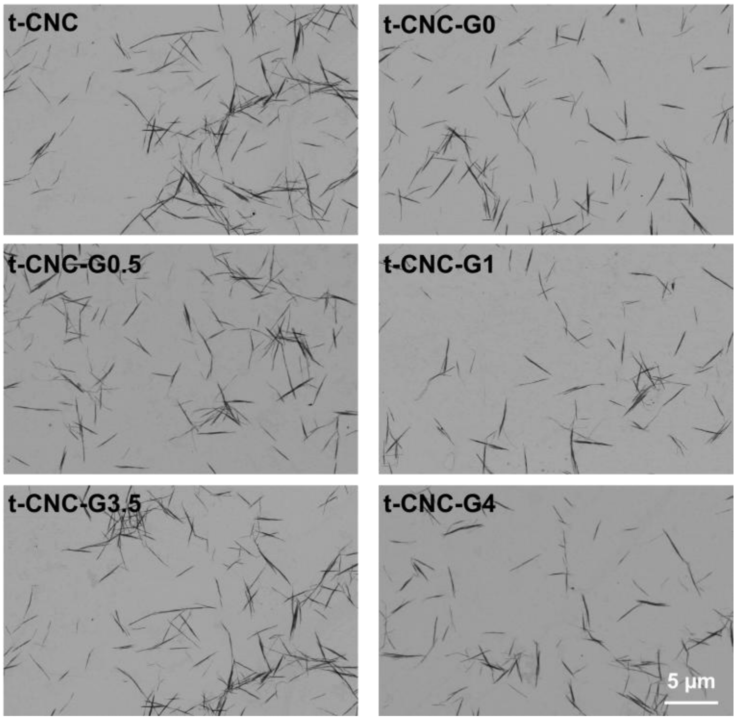

Fig. 2. STEM images of native t-CNC, amine-terminated (t-CNC-G0), the first acid- and amine-terminated (G0.5 and G1, respectively) and last acid- and amine-terminated (G3.5 and G4, respectively) dendrimer generations grown on t-CNC reducing ends.

The elemental compositions of t-CNC-G4 compared to native t-CNC (Table 1) revealed a significant higher nitrogen content for t-CNC-G4. According to the carbon-nitrogen (C/N) ratio, for t-CNC-G4 there was a nitrogen atom for each 45 glucose units. As the dendrimer G4 contains 62 nitrogen atoms, there was one dendrimer per 2800 glucose units. The degree of polymerization (DP) of cotton cellulose nanocrystals is between 150 and 325 (Potthast, A. et al., 2015); therefore, considering an elemental fibril formed by 16 cellulose chains and a high DP for tunicate nanocrystals, there was approximately 1.6 dendrimers for each cellulose nanocrystal. This high degree of substitution could be explained by the introduction of several dendrimer functionalities at the reducing end, or by some degree of chain breakdown during reactions that created new reducing ends.

Table 1

Elemental compositions and elemental C/N ratios for native t-CNC and t-CNC-G4. Determinations were made in triplicate and results are expressed as the mean ± standard deviation.

	N (%)	C (%)	S (%)	C/N
t-CNC	0.002 ± 0.002	43.925 ± 0.686	0.485 ± 0.169	9050 ± 764
t-CNC-G4	0.186 ± 0.002	43.090 ± 0.127	0.305 ± 0.064	232 ± 1

Fig. **3** shows the FTIR spectra of native t-CNC and t-CNC-G*x* for the first generations (G0.5 and G1) and the last ones (G3.5 and G4). The FTIR spectrum of native t-CNCs (green bottom trace) showed the characteristic bands of cellulose nanocrystals (Zhao, Y. & Li, J., 2014; Zhao, Y. D., Zhang, Y. J., Lindstrom, M. E., & Li, J. B., 2015). Upon dendrimer growth, the FTIR profile was not modified, which indicated that the crystalline order of t-CNC was not altered by reducing end modification.

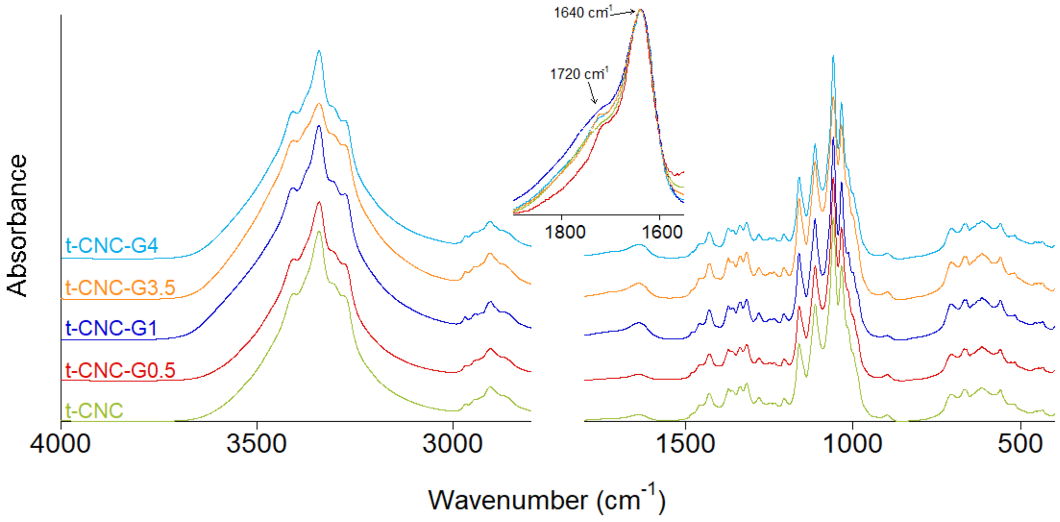

Fig. 3. FTIR spectra in absorbance of native t-CNC and the first acid- and amine-terminated (G0.5 and G1, respectively) and last acid- and amine-terminated (G3.5 and G4, respectively) dendrimer generations grown on t-CNC reducing ends.

The dendrimer growth was suggested by the increase in the C=O stretching band. For acid-terminated generations (G0.5 and G3.5), FTIR spectra showed a new peak at 1720 cm^{-1}, which corresponded to the C=O stretching band of COOH groups. The intensity of this band increased with generation, which pointed at dendritic growth. In the case of amine-terminated generations (G1 and G4), the peak from COOH had decreased in intensity compared to their precursors, indicating their partial transformation into amide forms. The spectra showed an increase in the shoulder intensity at 1700 cm^{-1}, which can be ascribed to the C=O stretching from amide I bonding at 1645 cm^{-1} (Benkaddour, A., Journoux-Lapp, C., Jradi, K., Robert, S., & Daneault, C., 2014). However, this small signal from the amide bonds would be overlapped with the band at 1635 cm^{-1} corresponding to the symmetric deformation vibration of adsorbed water molecules (Schwanninger, M., Rodrigues, J. C., Pereira, H., & Hinterstoisser, B., 2004). On the other hand, the bands of the C-N stretching and N-H deformation from amide II at 1545 cm^{-1} were not detected.

Dendritic growth was also demonstrated by the increase in the UV absorption band at 228 nm corresponding to TMA. Fig. **4** shows the absorbance spectra of a mixture of native t-CNC and TMA, and t-CNC-G0, t-CNC-G2 and t-CNC-G4.

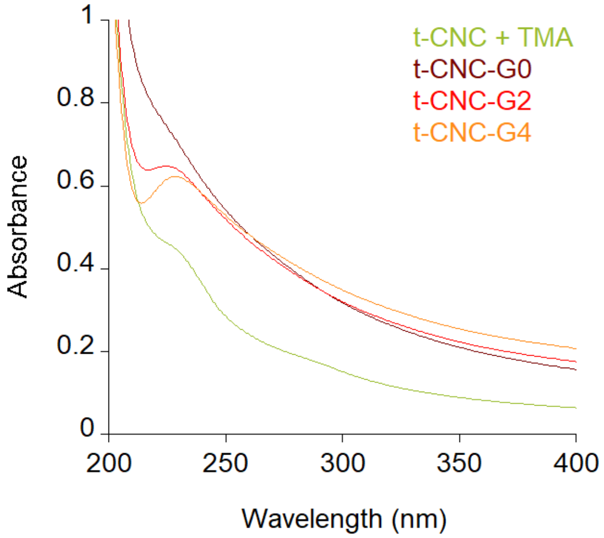

Fig. 4. Absorbance spectra of free TMA in a native t-CNC dispersion, and the dendrimer generations t-CNC-G0, t-CNC-G2 and t-CNC-G4.

The grafting of TMA on t-CNC resulted in an increasing baseline at low wavelengths possibly due to slight aggregation of nanocrystals, as well as the appearance of a shoulder at 280 nm ascribed to the TMA absorption band. When the generations increased, the shoulder at 280 nm become progressively more pronounced and, for the last generation, t-CNC-G4, a well-resolved band was observed. The possibility of unspecific adsorption of chemicals (HMDA and TMA) on the cellulose surface was discarded because in all cases, HMDA and TMA were added in high excess and t-CNC were thoroughly washed for their removal after reactions. Therefore, if chemicals were adsorbed on t-CNC we would not see the step-by-step increase of FTIR and UV absorption bands.

t-CNC-G4 was further studied by thermogravimetric analysis to compare with native t-CNC (Fig. **5**). The thermal analysis showed a two-step thermal degradation process, as previously described for cellulose nanocrystals (Lin, N. & Dufresne, A., 2014). First, the pyrolysis is catalyzed by the sulfate groups present on the t-CNC surface and then residues are carbonized (Wang, N., Ding, E. Y., & Cheng, R. S., 2007). The degradation profiles of native t-CNC and t-CNC-G4 were similar with a slight difference in the temperature that degradation started. For native t-CNC, thermal degradation started at 160 ºC whereas for t-CNC-G4 degradation began at 215 ºC, while it ended at 360 °C for both, meaning that the degradation of t-CNC-G4 is faster (confirmed by a much more intense peak for the differential thermogravimetric (DTG) curve). In the DTG curve, represented by the weight derivative (%/ºC), both native t-CNC and t-CNC-G4 showed prominent pyrolysis process with two step degradation processes at 295 and 495 ºC for native t-CNC and 293 and 480 ºC for t-CNC-G4. The slight but significant differences in the thermal stability profile when the dendrimers were synthesized at the reducing ends of t-CNC could be due to the dendrimer functionalization.

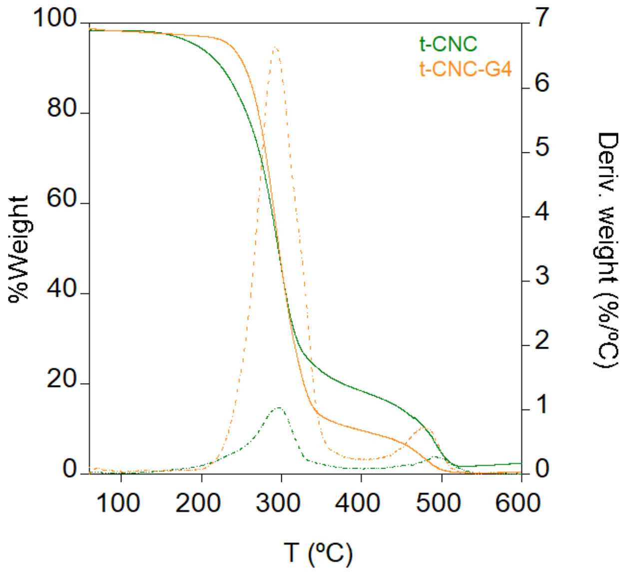

Fig. 5. Thermal gravimetric analysis (TGA) and first derivative of the TGA (differential thermogravimetric, DTG) curves of native t-CNC and t-CNC-G4.

3.2. Reducing-end driven supramolecular assembly

The affinity of amine groups for gold was used to demonstrate the dendrimer growth at the reducing ends of t-CNCs. Hence, the amine-terminated t-CNC-G0, t-CNC-G2 and t-CNC-G4 were adsorbed onto gold surfaces, and the adsorption process was monitored by surface plasmon resonance (SPR). SPR is an optical technique based on the resonant oscillation of conduction electrons at the interface between the gold surface and the t-CNC adsorbed layer when stimulated by incident light. Hence, when the gold surface is modified by t-CNC adsorption, the angle at which the plasmon is excited ($\Delta\theta$) changes (Ahola, S., Myllytie, P., Osterberg, M., Teerinen, T., & Laine, J., 2008). The adsorbed mass can be calculated from the SPR angle shift, according to Equation 1. Fig. **6** shows the adsorbed mass as a function of time for the adsorption of native t-CNC and the amine-terminated dendrimers t-CNC-G0, t-CNC-G2 and t-CNC-G4 onto gold surfaces.

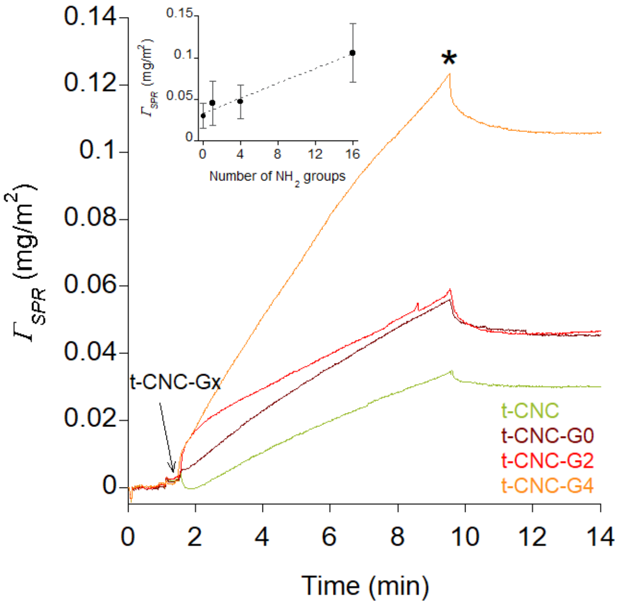

Fig. 6. Calculated surface coverage (Γ_{SPR}) from SPR angle shift as a function of time showing the adsorption of native t-CNC and the amine-terminated dendrimers t-CNC-G0, t-CNC-G2 and t-CNC-G4. The arrow indicates the injection and the asterisk the rinsing step. The inset depicts the relationship between surface coverage and the number of amine groups on the dendrimer.

The injection of native t-CNC resulted in a slight increase of the adsorbed mass, which indicated some unspecific and very limited adsorption onto the gold surface. The first generation t-CNC-G0 showed a similar profile to unmodified t-CNC but the surface coverage was higher. t-CNC-G0 only contained one amine group at the reducing end; therefore, the SPR profile could be due to a very slight adsorption on the gold surface. For t-CNC-G2, after injection, we observed a deep increase in the angle shift and therefore the adsorbed mass, even if at the end of the adsorption process, the surface coverage was similar to that of t-CNC-G0. Finally, the last generation t-CNC-G4 showed the largest increase in mass after injection that continued increasing towards a greater adsorbed mass. In all cases, the rinsing step resulted in a slight decrease of the adsorbed mass, indicating low t-CNC-G*x* desorption and demonstrating the stability of the adsorbed nanoparticles. The SPR results clearly demonstrated the dendrimer generation growth. Table 2 shows the surface coverage at the end of the adsorption process. In previous studies, we had demonstrated that the adsorption of reducing end-modified t-CNC was impacted by the probability of the nanocrystal to have the proper orientation to adsorb (Chemin, M. et al., 2020). Hence, reducing end-modified t-CNC should be rather perpendicular to the surface, with the reducing end close enough to the surface to facilitate interactions and the subsequent adsorption. The dendrimer generation growth increased the number of amino groups at the t-CNC reducing ends, increasing the size and therefore boosting the probability to encounter the surface. This assumption was demonstrated by the linear relationship between the number of amino groups and the surface coverage calculated by SPR (inset of Fig. **6**).

In order to get more insight into the arrangement of amine-terminated t-CNC-G*x* on the gold substrate, their adsorption was monitored by quartz crystal microbalance with dissipation (QCM-D). The evolution of frequency ($\Delta f_n/n$) and dissipation (ΔD_n) signals for the overtone number n = 5 as a function of time for t-CNC-G0, t-CNC-G2 and t-CNC-G4 dispersions are shown in Fig. **7**a and b. In all cases, the frequency decrease upon t-CNC-G*x* injection was very low (from -1 to -3 Hz), indicating a very small t-CNC-G*x* mass adsorbed on the gold substrate (Moreau, C., Beury, N., Delorme, N., & Cathala, B., 2012). In previous studies, we have already shown that unmodified CNC did not adsorb on gold substrates (Chemin, Maud et al., 2020; Villares, A. et al., 2018), which showed that the adsorption was driven by the functionalities at the reducing ends. The frequency decrease reflected the t-CNC-G*x* adsorbed mass together with the hydrating water. Therefore, the surface coverage calculated from QCM-D by the Sauerbrey's expression (equation 2) was in all cases higher than those calculated from SPR data (Table 2).

Table 2

Surface coverage calculated from SPR measurements (Γ_{SPR}) and QCM-D frequency (Γ_{QCM}) for the amine-terminated dendrimers t-CNC-G0, t-CNC-G2 and t-CNC-G4. Results are expressed as mean ± standard deviation

	Γ_{SPR} (mg m^{-2})	Γ_{QCM} (mg m^{-2})
t-CNC-G0	0.046 ± 0.026	0.296 ± 0.056
t-CNC-G2	0.047 ± 0.020	0.099 ± 0.054
t-CNC-G4	0.106 ± 0.036	0.187 ± 0.159

QCM-D allows monitoring dissipation changes concomitantly with frequency variations. Hence, the different viscoelastic nature of the adsorbed t-CNC-G*x* nanoparticles was investigated by the change of dissipation as a function of frequency (ΔD_n *vs* $\Delta f_n/n$). Fig. **7**c shows the ΔD_n *vs* $\Delta f_n/n$ plots for the adsorption of t-CNC-G0, -G2 and -G4. Usually, a small slope value of the ΔD_n *vs* $\Delta f_n/n$ curve indicates a relatively thin and rigid adsorbed layer whereas high slope values are characteristic of thicker and viscoelastic layers (Kishani, S., Vilaplana, F., Ruda, M., Hansson, P., & Wagberg, L., 2020; Rodahl, M. et al., 1997).

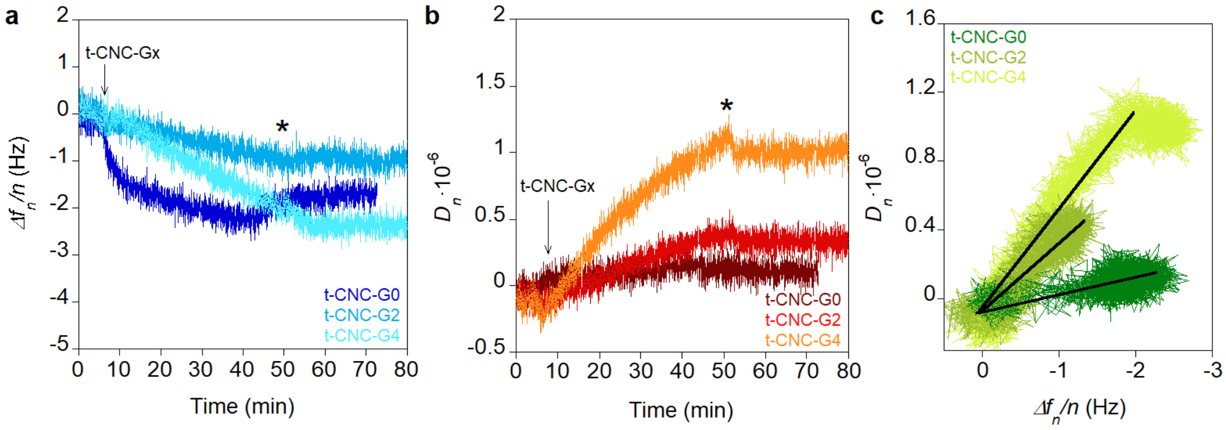

Fig. 7. Frequency ($\Delta f_n/n$) and dissipation (ΔD_n) changes for the overtone $n = 5$ monitored by QCM-D during adsorption of t-CNC-G0, t-CNC-G2 and t-CNC-G4: (a) frequency as a function of time; (b) dissipation as a function of time; and (c) ΔD_n *vs* $\Delta f_n/n$ plots. The arrow indicates the injection of t-CNCs and the asterisk the rinsing step.

The slopes values were 0.09, 0.33 and 0.49 · 10^{-6} Hz^{-1} for t-CNC-G0, t-CNC-G2 and t-CNC-G4, respectively. The increase in the slope values as the generation grew indicated higher viscoelasticity of the anchoring group for higher dendrimer generations. This illustrated that the dendrimer size and the number of peripheral amino groups at the reducing ends of t-CNC determined the viscoelastic properties and therefore the interaction between t-CNC-G*x* and the surface. Hence, as the generation increased, the t-CNC-G*x* could have more freedom to form more flexible layers. It has been previously postulated that the reducing end-modified CNC adsorb on the gold surface by their functionality at the reducing end, and repel each other electrostatically due to the sulfate groups on the CNC surface, resulting in a rather upright orientation (Chemin, Maud et al., 2020; Lokanathan, A. R. et al., 2013; Villares, A. et al., 2018). In previous studies on the “grafting onto” of PAMAM dendrimers on CNC reducing ends, we have observed an increase in the ΔD_n *vs* $\Delta f_n/n$ slope as the dendrimer generation increased (Chemin, Maud et al., 2020). In this study, we obtained similar slope values, and the gradual increase observed for t-CNC-G0 to t-CNC-G4 could point at a different adsorption regimes as the generation increased. Indeed, the generation growth results in a higher number of amino groups together with an increase of the dendrimer volume and flexibility compared to the rigid nanocrystal. This was reflected by the increasing dissipation values, which was a supplementary proof to demonstrate the dendrimer growth at the reducing end.

4. Discussion

The chemical polarity of cellulose nanocrystals has motivated the selective introduction of functionalities at only one end of the rod-like CNCs (Lin, F. et al., 2019; Lokanathan, A. R. et al., 2013; Villares, A. et al., 2018). The high reactivity of the aldehyde provides a specific anchoring point for chemical synthesis. Generally, macromolecules are introduced by “grafting onto” reactions, which involve coupling reactions between the terminal aldehyde and the targeted polymer (Chemin, Maud et al., 2020; Lin, F. et al., 2019; Sipahi-Saglam, E., Gelbrich, M., & Gruber, E., 2003; Tang, C. X. et al., 2018; Tao, H., Dufresne, A., & Lin, N., 2019; Tavakolian, M. et al., 2019). Differently, the “grafting from” approach includes the introduction of initiator molecules to carry out polymerization. Despite the advantages in terms of controllable polymerization and versatility of available monomers, the “grafting from” strategy has been scarcely used for polymer growth at the CNC reducing end. Zoppe et al. described for the first time the polymers synthesis at the reducing ends of CNC (Zoppe, J. O. et al., 2017). The introduction of initiators at reducing ends and the subsequent addition of the monomers *N*-isopropylacrylamide (NIPAM), [2-(methacryloyloxy)ethyl]-trimethylammonium chloride (METAC) and sodium 4-vinylbenzenesulfonate (4-SS) yielded nanorods with one end-tethered polymer chains by atom transfer radical polymerization (ATRP). By a similar approach, the same group described the polymerization of the thermoresponsive poly(*N*-isopropylacrylamide) (PNIPAM) at the reducing ends of CNC (Risteen, B. et al., 2018).

In this work, we describe for the first time the *in situ* growth of poly(amidoamine) dendrimers at the reducing end of cellulose nanocrystals. Our synthetic approach involved straightforward reactions in aqueous media and purification was easily achieved by phase separation. The growth of dendrimer generations was easily controlled by UV and FTIR spectroscopies, and we successfully introduced 4 generations. The better resolution of the FTIR band at 1720 cm^{-1} for the acid-terminated generations permitted to distinguish between the peripheral groups, amino or carboxylic acid, of each generation.

The divergent approach has been previously used for grafting dendrimers onto the whole CNC surface. Hence, poly(propylene imine) (PPI) and poly(amidoamine) (PAMAM) have been prepared up to the fourth generation. CNC were firstly aminated and dendrimer growth was performed by iterative Michael additions (Golshan, M. et al., 2017; Hassan, M. L., 2006; Tehrani, A. D. & Basiryan, A., 2015; Wang, Y. C. & Lu, Q. Y., 2020). The grafting density in terms of amino groups was 20.1 mmol g^{-1} for the fourth PPI generation (Golshan, M. et al., 2017) and 3.54 mmol g^{-1} for the fourth PAMAM generation (Wang, Y. C. & Lu, Q. Y., 2020), both at the CNC surface. In both cases, the coverage of the CNC surface by the dendrimer moieties was high, which resulted in CNC aggregation (Golshan, M. et al., 2017; Wang, Y. C. & Lu, Q. Y., 2020). The advantage of growing dendrimers specifically at the reducing end is the possibility of preserving the CNC surface properties but introducing new functionalities at only one end. Furthermore, this patchy functionalization allows the supramolecular assembly of CNC by their reducing end, even if the grafting density was significantly lower (0.14 mmol g^{-1}), resulting in hairy layers (Lokanathan, A. R. et al., 2013). Hence, this work demonstrates that the reducing end dendrimer-grafting allowed the adsorption of t-CNC-G*x* onto gold surfaces by their modified reducing end. This is of special importance for designing novel materials by supramolecular assembly where CNC can be specifically bound by one end.

5. Conclusions

This work describes a straightforward "grafting onto" strategy to synthesize poly(amidoamine) dendrimers at the reducing ends of tunicate cellulose nanocrystals. The generation growth was monitored by UV and FTIR spectroscopies. This work demonstrates that SPR and QCM-D are suitable techniques for detecting functionalities at the nanocrystal reducing ends, and the ΔD_n *vs* $\Delta f_n/n$ plots allow to discern the arrangement of nanocrystals at the gold surface. Concluding, cellulose nanocrystals can be viewed as a good strategy for the step-by-step synthesis of polymers, especially dendrimers since they act as a solid support that facilitates dendrimer purification. Indeed, the presence of dendritic structures at the reducing ends dictates their interaction with gold surfaces, and increase the versatility of cellulose materials.

Acknowledgements

This work was financially supported by the French National Research Agency (Project Cellmach, ANR-17-CE07-0010-01). We greatly thank Dr. Hervé Bizot for the preparation of tunicate nanocrystals. The authors acknowledge the technical support on DSC from Jean-Eudes Maigret and the BIBS platform of INRAE for the access to infrared spectroscopy (Sylvie Durand) and microscopy facilities (Bruno Novales and Angelina D'Orlando).

Declaration of competing interest

The authors declare no conflicts of interest.

References

Ahola, S., Myllytie, P., Osterberg, M., Teerinen, T., & Laine, J. (2008). Effect of polymer adsorption on cellulose nanofibril water binding capacity and aggregation. *Bioresources,* 3(4), 1315-1328.

Benkaddour, A., Journoux-Lapp, C., Jradi, K., Robert, S., & Daneault, C. (2014). Study of the hydrophobization of TEMPO-oxidized cellulose gel through two routes: amidation and esterification process. *Journal of Materials Science,* 49, 2832-2843.

Charreau, H., Cavallo, E., & Foresti, M. L. (2020). Patents involving nanocellulose: Analysis of their evolution since 2010. *Carbohydrate Polymers,* 237.

Chemin, M., Moreau, C., Cathala, B., & Villares, A. (2020). Adsorption Behavior of Reducing End-Modified Cellulose Nanocrystals: A Kinetic Study Using Quartz Crystal Microbalance. *Journal of Renewable Materials,* 8(1), 29-43.

Chemin, M., Moreau, C., Cathala, B., & Villares, A. (2020). Asymmetric modification of cellulose nanocrystals with PAMAM dendrimers for the preparation of pH-responsive hairy surfaces. *Carbohydrate Polymers,* 249, 116779.

Delepierre, G., Heise, K., Malinen, K., Koso, T., Pitkänen, L., Cranston, E. D., . . . King, A. W. T. (2021). Challenges in Synthesis and Analysis of Asymmetrically Grafted Cellulose Nanocrystals via Atom Transfer Radical Polymerization. *Biomacromolecules,* 22(6), 2702-2717.

Eichhorn, S. J. (2011). Cellulose nanowhiskers: promising materials for advanced applications. *Soft Matter,* 7(2), 303-315.

Golshan, M., Salami-Kalajahi, M., Roghani-Mamaqani, H., & Mohammadi, M. (2017). Poly(propylene imine) dendrimer-grafted nanocrystalline cellulose: Doxorubicin loading and release behavior. *Polymer,* 117, 287-294.

Guo, Y. Q., Shen, M. W., & Shi, X. Y. Construction of Poly(amidoamine) Dendrimer/Carbon Dot Nanohybrids for Biomedical Applications. *Macromolecular Bioscience*.

Hassan, M. L. (2006). Preparation and thermal stability of new cellulose-based poly(propylene imine) and poly(amido amine) hyperbranched derivatives. *Journal of Applied Polymer Science,* 101(3), 2079-2087.

Heise, K., Delepierre, G., King, A., Kostiainen, M., Zoppe, J., Weder, C., & Kontturi, E. (2020). Chemical modification of cellulose nanocrystal reducing end-groups. *Angewandte Chemie International Edition,* 60(1), 66-87.

Heise, K., Kontturi, E., Allahverdiyeva, Y., Tammelin, T., Linder, M. B., Nonappa, & Ikkala, O. (2020). Nanocellulose: Recent Fundamental Advances and Emerging Biological and Biomimicking Applications. *Advanced Materials,* 33(3), 2004349.

Kishani, S., Vilaplana, F., Ruda, M., Hansson, P., & Wagberg, L. (2020). Influence of Solubility on the Adsorption of Different Xyloglucan Fractions at Cellulose-Water Interfaces. *Biomacromolecules,* 21(2), 772-782.

Kontturi, K. S., Kontturi, E., & Laine, J. (2013). Specific water uptake of thin films from nanofibrilar cellulose. *Journal of Materials Chemistry A,* 1, 13655-13663.

Lin, F., Cousin, F., Putaux, J.-L., & Jean, B. (2019). Temperature-Controlled Star-Shaped Cellulose Nanocrystal Assemblies Resulting from Asymmetric Polymer Grafting. *Acs Macro Letters,* 8, 345-351.

Lin, N., & Dufresne, A. (2014). Surface chemistry, morphological analysis and properties of cellulose nanocrystals with gradiented sulfation degrees. *Nanoscale,* 6(10), 5384-5393.

Lin, N., Huang, J., Chang, P. R., Anderson, D. P., & Yu, J. (2011). Preparation, Modification, and Application of Starch Nanocrystals in Nanomaterials: A Review. *Journal of Nanomaterials*.

Lokanathan, A. R., Lundahl, M., Rojas, O. J., & Laine, J. (2014). Asymmetric cellulose nanocrystals: thiolation of reducing end groups via NHS-EDC coupling. *Cellulose,* 21(6), 4209-4218.

Lokanathan, A. R., Nykanen, A., Seitsonen, J., Johansson, L.-S., Campbell, J., Rojas, O. J., . . . Laine, J. (2013). Cilia-Mimetic Hairy Surfaces Based on End-Immobilized Nanocellulose Colloidal Rods. *Biomacromolecules,* 14(8), 2807-2813.

Moreau, C., Beury, N., Delorme, N., & Cathala, B. (2012). Tuning the architecture of cellulose nanocrystal-poly(allylamine hydrochloride) multilayered thin films: Influence of dipping parameters. *Langmuir,* 28(28), 10425-10436.

Nikzamir, M., Hanifehpour, Y., Akbarzadeh, A., & Panahi, Y. Applications of Dendrimers in Nanomedicine and Drug Delivery: A Review. *Journal of Inorganic and Organometallic Polymers and Materials*.

Potthast, A., Radosta, S., Saake, B., Lebioda, S., Heinze, T., Henniges, U., . . . Wetzel, H. (2015). Comparison testing of methods for gel permeation chromatography of cellulose: coming closer to a standard protocol. *Cellulose,* 22(3), 1591-1613.

Risteen, B., Delepierre, G., Srinivasarao, M., Weder, C., Russo, P., Reichmanis, E., & Zoppe, J. (2018). Thermally Switchable Liquid Crystals Based on Cellulose Nanocrystals with Patchy Polymer Grafts. *Small,* 14(46).

Rodahl, M., Hook, F., Fredriksson, C., Keller, C. A., Krozer, A., Brzezinski, P., . . . Kasemo, B. (1997). Simultaneous frequency and dissipation factor QCM measurements of biomolecular adsorption and cell adhesion. *Faraday Discussions,* 107, 229-246.

Sacui, I. A., Nieuwendaal, R. C., Burnett, D. J., Stranick, S. J., Jorfi, M., Weder, C., . . . Gilman, J. W. (2014). Comparison of the Properties of Cellulose Nanocrystals and Cellulose Nanofibrils Isolated from Bacteria, Tunicate, and Wood Processed Using Acid, Enzymatic, Mechanical, and Oxidative Methods. *Acs Applied Materials & Interfaces,* 6(9), 6127-6138.

Sauerbrey, G. (1959). Verwendung von Schwingquarzen zur Wägung dünner Schichten und zur Mikrowägung. *Zeitschrift für Physik,* 155(2), 206-222.

Schoch, R. L., & Lim, R. Y. H. (2013). Non-Interacting Molecules as Innate Structural Probes in Surface Plasmon Resonance. *Langmuir,* 29(12), 4068-4076.

Schwanninger, M., Rodrigues, J. C., Pereira, H., & Hinterstoisser, B. (2004). Effects of short-time vibratory ball milling on the shape of FT-IR spectra of wood and cellulose. *Vibrational Spectroscopy,* 36(1), 23-40.

Shea, F., & Watts, C. E. (1939). Dumas method for organic nitrogen. *Industrial and Engineering Chemistry Analytical Edition,* 11(6), 333-334.

Sipahi-Saglam, E., Gelbrich, M., & Gruber, E. (2003). Topochemically modified cellulose. *Cellulose,* 10(3), 237-250.

Tang, C. X., Spinney, S., Shi, Z. Q., Tang, J. T., Peng, B. L., Luo, J. H., & Tam, K. C. (2018). Amphiphilic Cellulose Nanocrystals for Enhanced Pickering Emulsion Stabilization. *Langmuir,* 34(43), 12897-12905.

Tao, H., Dufresne, A., & Lin, N. (2019). Double-Network Formation and Mechanical Enhancement of Reducing End-Modified Cellulose Nanocrystals to the Thermoplastic Elastomer Based on Click Reaction and Bulk Cross-Linking. *Macromolecules,* 52(15), 5894-5906.

Tao, H., Lavoine, N., Jiang, F., Tang, J., & Lin, N. (2020). Reducing end modification on cellulose nanocrystals: strategy, characterization, applications and challenges. *Nanoscale Horizons,* 5(4), 607-627.

Tavakolian, M., Lerner, J., Tovar, F. M., Frances, J., van de Ven, T. G. M., & Kakkar, A. (2019). Dendrimer directed assembly of dicarboxylated hairy nanocellulose. *Journal of Colloid and Interface Science,* 541, 444-453.

Tehrani, A. D., & Basiryan, A. (2015). Dendronization of cellulose nanowhisker with cationic hyperbranched dendritic polyamidoamine. *Carbohydrate Polymers,* 120, 46-52.

Terech, P., Chazeau, L., & Cavaille, J. Y. (1999). A small-angle scattering study of cellulose whiskers in aqueous suspensions. *Macromolecules,* 32(6), 1872-1875.

Villares, A., Moreau, C., & Cathala, B. (2018). Star-like Supramolecular Complexes of Reducing-End-Functionalized Cellulose Nanocrystals. *Acs Omega,* 3(11), 16203-16211.

Wang, N., Ding, E. Y., & Cheng, R. S. (2007). Thermal degradation behaviors of spherical cellulose nanocrystals with sulfate groups. *Polymer,* 48(12), 3486-3493.

Wang, Y. C., & Lu, Q. Y. (2020). Dendrimer functionalized nanocrystalline cellulose for Cu(II) removal. *Cellulose,* 27(4), 2173-2187.

Zhao, Y., & Li, J. (2014). Excellent chemical and material cellulose from tunicates: diversity in cellulose production yield and chemical and morphological structures from different tunicate species. *Cellulose,* 21(5), 3427-3441.

Zhao, Y. D., Zhang, Y. J., Lindstrom, M. E., & Li, J. B. (2015). Tunicate cellulose nanocrystals: Preparation, neat films and nanocomposite films with glucomannans. *Carbohydrate Polymers,* 117, 286-296.

Zoppe, J. O., Dupire, A. V. M., Lachat, T. G. G., Lemal, P., Rodriguez-Lorenzo, L., Petri-Fink, A., . . . Klok, H.-A. (2017). Cellulose Nanocrystals with Tethered Polymer Chains: Chemically Patchy versus Uniform Decoration. *Acs Macro Letters,* 6(9), 892-897.